

Simultaneous control of composition, size and morphology in discrete Ni_{2-x}CoxP nanoparticles

D. Ruchira Liyanage, Samuel J Danforth, Yi Liu, Mark E Bussell, and Stephanie L. Brock

Chem. Mater., **Just Accepted Manuscript** • DOI: 10.1021/acs.chemmater.5b00958 • Publication Date (Web): 20 May 2015

Downloaded from <http://pubs.acs.org> on May 31, 2015

Just Accepted

“Just Accepted” manuscripts have been peer-reviewed and accepted for publication. They are posted online prior to technical editing, formatting for publication and author proofing. The American Chemical Society provides “Just Accepted” as a free service to the research community to expedite the dissemination of scientific material as soon as possible after acceptance. “Just Accepted” manuscripts appear in full in PDF format accompanied by an HTML abstract. “Just Accepted” manuscripts have been fully peer reviewed, but should not be considered the official version of record. They are accessible to all readers and citable by the Digital Object Identifier (DOI®). “Just Accepted” is an optional service offered to authors. Therefore, the “Just Accepted” Web site may not include all articles that will be published in the journal. After a manuscript is technically edited and formatted, it will be removed from the “Just Accepted” Web site and published as an ASAP article. Note that technical editing may introduce minor changes to the manuscript text and/or graphics which could affect content, and all legal disclaimers and ethical guidelines that apply to the journal pertain. ACS cannot be held responsible for errors or consequences arising from the use of information contained in these “Just Accepted” manuscripts.

Simultaneous control of composition, size and morphology in discrete $\text{Ni}_{2-x}\text{Co}_x\text{P}$ nanoparticles

D. Ruchira Liyanage,¹ Samuel J. Danforth,² Yi Liu,^{3†} Mark E. Bussell² and Stephanie L Brock^{1,*}

1. Department of Chemistry, Wayne State University, Detroit Michigan 48202, (USA)

2. Department of Chemistry, Western Washington University, Bellingham, WA 98225 (USA)

3. Electron Microscopy Facility, Oregon State University, Corvallis Oregon 97331 (USA). [†]Present address: Technical Center, Chrysler LLC, 2301 Feather Stone Road, Auburn Hills, MI 48326 (USA)

ABSTRACT: A synthetic protocol developed to produce phase-pure, nearly monodisperse $\text{Ni}_{2-x}\text{Co}_x\text{P}$ nanoparticles ($x \leq 1.7$) is described. The $\text{Ni}_{2-x}\text{Co}_x\text{P}$ particles vary in size, ranging from 9-14 nm with standard deviations of <20% (based on TEM analysis) and the actual metal ratios obtained from EDS closely follow the targeted ratios. With increasing Co, samples with larger size distributions are obtained and include particles with voids, attributed to the Kirkendall effect. In order to probe the mechanism of ternary phosphide particle formation, detailed studies were conducted for Ni:Co = 1:1 as a representative composition. It was revealed that the P:M ratio, heating temperature and heating time have a large impact on the nature of both intermediate and final crystalline particles formed. By tuning these conditions, nanoparticles can be produced with different sizes (from ca 7-25 nm) and morphology (hollow vs. dense).

Introduction

Transition metal phosphides are an important class of materials for applications in energy storage,¹ optics,² magnetism,³ and catalysis.^{4,5} With respect to catalysis, transition metal phosphides are being evaluated for both hydrodesulfurization (HDS) and hydrogen evolution reaction (HER) processes, among others.⁶⁻¹¹ While binary phases have been extensively studied,^{6,10,12} only recently have researchers started to explore opportunities for synergism afforded by ternary phases.¹³⁻¹⁶ Ternary phosphides of formula $\text{Ni}_{2-x}\text{Co}_x\text{P}$ are of particular interest as they have shown improved HDS activity relative to the best of the binary phases (Ni_2P) for low concentrations of Co ($x \leq 0.1$).^{14,17} Likewise Zhang and co-workers observed $\text{Ni}_{2-x}\text{Co}_x\text{P}$ to be an active catalyst for hydrazine decomposition, with the highest activity observed for the $\text{Ni}_{1.0}\text{Co}_{1.0}\text{P}_{1.5}$ composition.¹⁵ While these studies point to the promise of these phases as active catalysts with a range of potential applications, the lack of synthetic methodologies enabling nanoparticle formation with independent tuning of composition and size impedes the development of a comprehensive model for their function.

In contrast to traditional methods of preparing heterogeneous catalysts (incipient wetness, temperature pro-

grammed reduction, etc.), solution-phase arrested-precipitation reactions enable excellent control of size, shape and composition, producing samples comprising narrowly polydisperse, discrete nanoparticles.¹⁸⁻²¹ This approach has been extensively employed for the synthesis of binary phosphides, and these have recently been demonstrated to be effective as model catalysts for HDS^{22,23} as well as electrocatalysts for HER.⁶⁻¹⁰ In contrast, few examples of arrested precipitation reactions delivering ternary phosphide nanoparticles are reported.^{24,25} Such reports often target a limited range of composition space and do not perform the systematic evaluation needed to control the reaction characteristics to yield targeted size, composition, and shape. To our knowledge, reports of discrete $\text{Ni}_{2-x}\text{Co}_x\text{P}$ nanoparticles are limited to a 2014 report by Peng and co-workers on the synthesis of $\text{Co}_{1.33}\text{Ni}_{0.67}\text{P}$ nanorods. This material proved to be active for HER,¹⁶ underscoring the need for a rational synthetic approach that would enable tuning of catalytic function in ternary phosphide nanoparticles by independently addressing size, shape and composition.

In this work, a protocol to synthesize narrow polydispersity phase-pure $\text{Ni}_{2-x}\text{Co}_x\text{P}$ nanoparticles for different compositions ($x \leq 1.7$) is established. The role of reaction temperature, initial precursor ratio and heating times on the resultant size, composition and shape of the products

will be presented. Thus, in addition to providing a route to new materials for catalytic testing, this paper also contributes to our fundamental knowledge of the operations of synthetic levers in control of phase and composition for transition metal phosphide nanoparticles.

Experimental Section

Materials

Nickel acetylacetonate (95%) was purchased from Alfa Aesar, cobalt(II) acetylacetonate (99%) was purchased from Sigma-Aldrich, n-octyl ether (95%) and oleylamine (>50%) were purchased from TCI America, tri-n-octylphosphine (TOP, 97%) was purchased from STREM Chemicals, chloroform was purchased from Fisher Scientific, and methanol and ethanol (200 proof) were purchased from Decon laboratories. All chemicals were used as received. The purity of oleylamine was assessed by NMR (Figure S1) and it was determined that impurities consist largely of other saturated and unsaturated primary amines.

Synthesis of $\text{Ni}_{2-x}\text{Co}_x\text{P}$ nanoparticles ($0 \leq x \leq 2$)

All reactions were carried out under argon atmosphere using standard Schlenk line techniques. In a typical synthesis, the corresponding amounts (overall 2.0 mmol) of the two metal precursors ($\text{Ni}(\text{acac})_2$, $\text{Co}(\text{acac})_2$) were combined with 5.0 mL (8.0 mmol) of oleylamine (coordinating ligand), 10.0 mL of octyl ether (solvent) and 4.0 mL (10.0 mmol) of trioctylphosphine (TOP, P source) in a 200 mL Schlenk flask with a condenser. The flask was placed on a heating mantle operated by a temperature controller and the thermocouple was inserted between the flask and the heating mantle. The flask was thermally insulated by wrapping with glass wool. The mixture was degassed at 110 °C for 20 min to remove any moisture or oxygen, followed by purging with argon for 20 min at this temperature (the reaction is conducted under slight positive pressure of Ar). The temperature was then increased to 230 °C and maintained for 90 min. Next, the temperature was set to heat rapidly (ca 40 °C/min) to 350 °C; as soon as the temperature started increasing, a 6 mL (15 mmol) aliquot of TOP was injected, followed by heating for 4.5 h at 350 °C. The black product was isolated by precipitation with ethanol. The product was dispersed again in chloroform, sonicated for 5-10 min and reprecipitated with ethanol. This sonication and precipitation process was carried out at least three times.

Characterization

Powder X-ray diffraction (PXRD) patterns were collected on a Rigaku RU 200B diffractometer with $\text{Cu K}\alpha$ radiation (0.154 nm) operated at 40kV, 150mA. Samples were deposited on a zero background quartz holder using minimal grease and data were collected over the 2θ range 30-80°. Silicon was used as an internal 2θ standard. The patterns were compared to powder diffraction files (PDFs)

from the ICDD database for phase identification. The collected patterns were analyzed using Jade 5.0 software for crystallite size (using the Scherrer equation), while analyses of the patterns using the Rietveld method were carried out using PANalytical HighScore Plus software. Co fluorescence incited by the Cu radiation results in significant noise, and hence a diminished spectrum quality, in data acquired on Co-rich samples.

Transmission electron microscopy (TEM) and energy dispersive spectroscopy (EDS) were carried out with a JEOL 2010 electron microscope operating at a voltage of 200 kV and coupled to an EDS detector (EDAX Inc). Bright field images were captured by Amtv 600 software. TEM specimens were prepared by dispersion of nanoparticles in chloroform and depositing a drop of solution on a formvar carbon coated 200 mesh Cu grid, followed by drying in air. The peak positions in the EDS were calibrated using Al (1.486 keV) and Cu (8.040 keV) metals. The particle sizes were analyzed by NIS-Elements D3.10 software. The spherical boundary of a particle was assigned by manually selecting 3 points on the edge of each particle. To obtain the histograms, the sizes of particles obtained were categorized into 0.2 nm bin sizes. EDS elemental mappings were collected using an FEI Titan 80-200 scanning transmission electron microscope (STEM) with ChemiSTEM technology operated at 200 kV. The STEM images were taken using a high angle annular dark field detector (HAADF). The so-called "Super X" EDS system, which includes 4 windowless silicon-drift detectors (SDD) around the specimen made by Bruker Corporation, provides a solid angle of more than 0.9 srad, and the X-ray signal is usually more than 1000 cps at a magnification of about 640,000x.

X-ray photoelectron spectroscopy (XPS) analyses were carried out using a Surface Science Instruments S-probe spectrometer. This instrument has a monochromatized Al $\text{K}\alpha$ X-ray source and a low energy electron flood gun for charge neutralization of non-conducting samples. The samples were dusted onto double-sided tape and run as insulators. X-ray spot size for these acquisitions was approximately 800 μm . Pressure in the analytical chamber during spectral acquisition was less than 5×10^{-9} Torr. The pass energy for survey spectra (to calculate composition) was 150 eV and the pass energy for high resolution scans was 50 eV. The binding energy scales of the high-resolution spectra were calibrated by assigning the most intense C_{1s} high-resolution peak a binding energy of 285.0 eV.

Results and Discussion

The protocol developed to synthesize $\text{Ni}_{2-x}\text{Co}_x\text{P}$ nanoparticles is based on the method refined by our group to synthesize discrete Ni_2P phase-pure nanoparticles.²⁰ To make the binary nanoparticles, Ni and Co acetylacetonate (acac) complexes are combined at the outset of the reac-

tion with trioctylphosphine (TOP) in a solution of octyl ether and oleylamine (OA) as shown in Scheme 1. This was heated to 230°C to prepare the Ni-Co-P alloy precursor particles, which are then converted to the crystalline ternary phosphide by adding an additional aliquot of TOP and heating to 350°C. In the original Ni₂P study, we observed that the initial TOP:M:OA=10.0:2.0:8.0 molar ratio resulted in nearly monodisperse ($\pm 20\%$ S.D., in the terminology coined by Finke²⁶) and discrete amorphous intermediate Ni_xP_y precursor particles. Accordingly, in all the Ni, Co compositions targeted, the initial molar ratio was set to TOP:M:OA = 10.0:2.0:8.0 while the final TOP:M ratio was increased to 11.2 by injecting an additional 6.0 mL of TOP at 350°.

Structural, morphological and surface chemical changes of ternary phosphide nanoparticles with composition

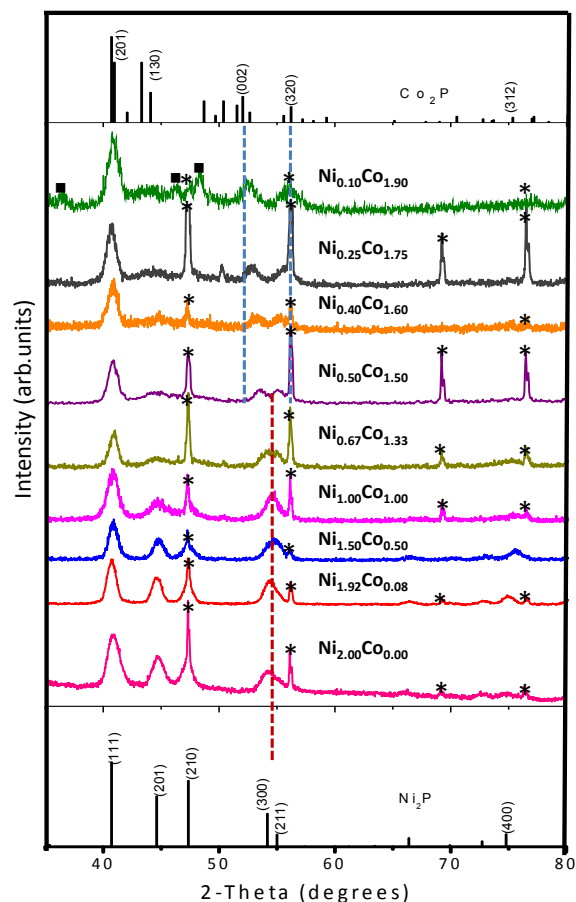


Figure 1. PXRD patterns for different targeted compositions of Ni_{2-x}Co_xP. Reference patterns for Co₂P and Ni₂P are shown for comparison with drop lines indicating the major distinguishing peaks for the two phases. The sharp peaks denoted with * arise from an internal Si standard. Peaks denoted with ■ arise from a CoP impurity.

The products of the different targeted compositions obtained were characterized for phase by PXRD, morphology by TEM, and composition by EDS. Figure 1 illustrates the PXRD patterns for different targeted compositions.

Ni₂P and Co₂P adopt the hexagonal Fe₂P and orthorhombic Co₂P structure-types, respectively. Both have two metal sites, M(1) and M(2) with tetrahedral and square pyramidal geometries, respectively, defined by P. However, the two structures differ in the packing of rhombohedral subcells containing M(1) and M(2) sites within the crystal (Figure 2). Each P atom is in a tri-capped trigonal prismatic geometry defined by Ni atoms.

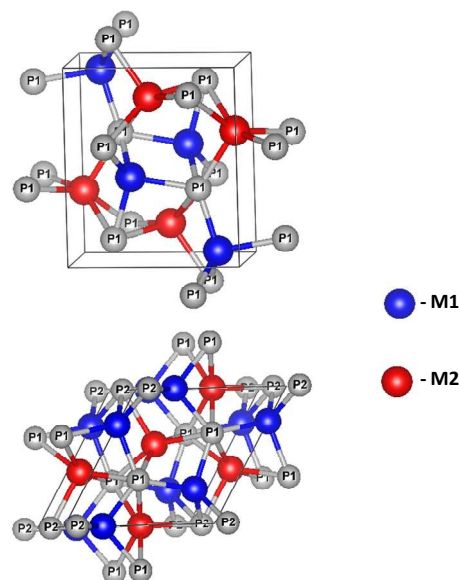


Figure 2. Orthorhombic Co₂P structure-type (top) hexagonal Fe₂P structure-type (bottom).

In Figure 1 the patterns match the Ni₂P (hexagonal) structure in the nickel rich region and this phase is clearly maintained up to a targeted composition of Ni_{0.67}Co_{1.33}P, at which point we observed a change in the pattern. For the nickel rich compositions, there is a broad peak near 55° 2θ corresponding to the overlapping reflections of (300) and (211) planes. Due to the small size of the crystallites these two peaks overlap, resulting in one broad peak. However, for the composition Ni_{0.67}Co_{1.33}P, we observed the appearance of two peaks that shift away from each other as the Co is increased. This splitting can be attributed to a separation of the (300) and (211) reflections upon Co-incorporation, or a shift to the Co₂P structure type. Importantly, all observed peaks for compositions up to x=1.75, could be assigned to the desired ternary phase, suggesting that homogeneous materials can be prepared in this composition space (i.e., no detectable crystalline impurities are present). However, at the very Co-rich end (x=1.9), CoP is observed

as an impurity. Likewise, this methodology is unsuccessful at preparing phase pure Co_2P ; attempts to do so produce a mixture of Co_2P , CoP and unidentified impurities (Figure S2).

Table 1. Ni:Co target and actual (as assessed by EDS) metal ratios, crystallite sizes (by Scherrer application to PXRD data), particle size (by TEM) and refined lattice parameters for different compositions of $\text{Ni}_{2-x}\text{Co}_x\text{P}$

Target ratio (Ni:Co)	Actual ratio (Ni:Co)	Crystallite size (nm)	TEM size (nm)	Lattice parameters (Å)					Molecular Volume (Å ³) ^a
				Ni ₂ P type refined		Co ₂ P type refined			
				A	c	a	b	c	
2.00 : 0.00	2.00 : 0.00	9.1	11.26±0.34	5.889(5)	3.364(2)	-	-	-	33.69
1.92 : 0.08	1.91 : 0.09	10.3	12.36±0.65	5.877(9)	3.372(3)	-	-	-	33.62
1.50 : 0.50	1.52 : 0.48	9.6	11.09±0.97	5.877(5)	3.354(3)	-	-	-	33.43
1 : 1	1.06 : 0.94	8.1	9.77±0.94	5.853(6)	3.381(3)	-	-	-	33.44
0.67 : 1.33	0.71 : 1.29	10.9	13.28±2.04	5.824(9)	3.398(4)	-	-	-	33.27
0.5 : 1.5	0.55 : 1.45	10.0	12.73±1.98	-	-	5.851(9)	6.530(7)	3.414(6)	32.62
0.4 : 1.6	0.44 : 1.56	9.1	11.57±2.07	-	-	5.83(3)	6.44(3)	3.42(2)	31.98
0.25 : 1.75	0.29 : 1.71	9.5	12.5±1.88	-	-	5.801(7)	6.468(5)	3.443(3)	32.30

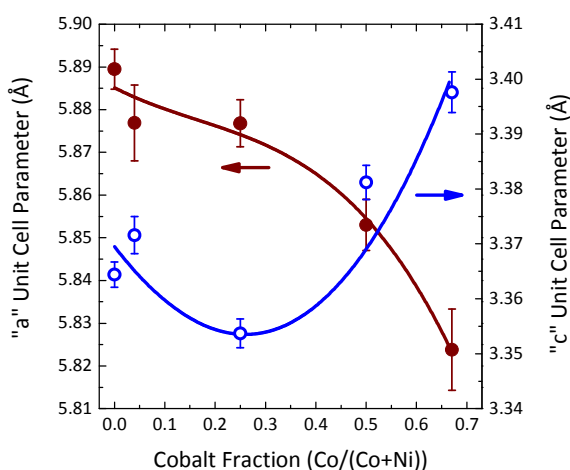


Figure 3. Hexagonal unit cell parameters (Ni_2P structure) plotted as a function of the Co content (polynomial fits are guides for the eye).

All the phase pure PXRD patterns were calibrated using silicon as an internal standard. Crystallite sizes were calculated by application of the Scherrer equation to the most intense peak, around 41° , corresponding to the (111) plane of Ni_2P or to the overlapping (121), (201) planes of Co_2P (Table 1). The crystallite sizes range from 8-11 nm with no discernible size trends based on composition.

The PXRD patterns were analyzed using the Rietveld refinement method in order to determine the lattice

constants for the phase-pure $\text{Ni}_{2-x}\text{Co}_x\text{P}$ materials (Figure S3). The refined lattice constants and molecular volumes (Ni_2P structure: (unit cell volume)/3; Co_2P structure: (unit cell volume)/4) are listed in Table 1. For nominal compositions $x < 1.5$, the PXRD patterns were refined starting from the Ni_2P structure (PDF#74-1385) and good fits were obtained. However, attempts to refine the $x = 1.5$ composition on the hexagonal structure resulted in a poorer quality fit of the pattern. Thus for the three most Co rich compositions, refinement was carried out based on the Co_2P structure (PDF#32-0306), resulting in a notable improvement in the fit and more reasonable lattice parameters. Intriguingly, the phase transformation appears at a somewhat more Ni-rich composition in our nanoparticles than is reported for the bulk material ($x = 1.7$),²⁷⁻²⁹

The unit cell parameters for the $\text{Ni}_{2-x}\text{Co}_x\text{P}$ materials adopting the Ni_2P structure ($x < 1.5$) are consistent with those reported for bulk phases of similar composition,²⁷⁻²⁹ and exhibit clear trends as a function of Co content as shown in Figure 3. The “a” lattice parameter decreases with increasing Co content while the “c” lattice parameter shows a minimum for the $\text{Ni}_{1.50}\text{Co}_{0.50}\text{P}$ composition. The orthorhombic unit cell parameters for the three most Co-rich compositions, which were fitted based on the Co_2P structure, are also consistent with those for bulk phase $\text{Ni}_{2-x}\text{Co}_x\text{P}$ materials.²⁷⁻²⁹ Except for the $\text{Ni}_{0.4}\text{Co}_{1.6}\text{P}$ composition, which yielded the poorest fit, the molecular volumes calculated for the nanoparticle samples (Table 1) using the results of the Rietveld refinement analyses are in excellent agreement with those noted previously for bulk

phase $\text{Ni}_{2-x}\text{Co}_x\text{P}$ materials over the entire composition range investigated ($0 \leq x \leq 1.75$).²⁷ The unusual trend observed for the hexagonal unit cell parameters, with “c” exhibiting a minimum value near the composition $\text{Ni}_{1.50}\text{Co}_{0.50}\text{P}$, has been attributed previously to ordering of the metal atoms in the M(1) and M(2) sites.

Neutron diffraction measurements carried out on bulk phase $\text{Ni}_{2-x}\text{Co}_x\text{P}$ materials ($x = 0.8, 1.0, 1.2$) showed a strong preference for Ni atoms to occupy the square pyramidal (M(2)) sites,³⁰ which is unexpected based on atomic size (covalent radii: Ni - 121 pm, Co - 126 pm).³¹

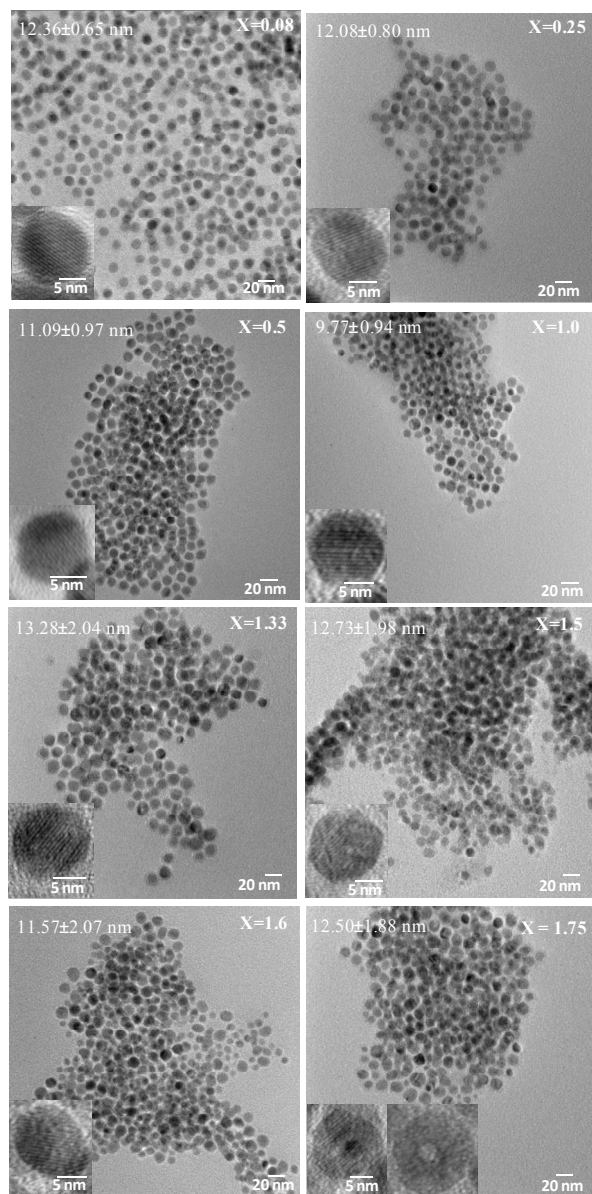


Figure 4. TEM images for $\text{Ni}_{2-x}\text{Co}_x\text{P}$ nanoparticles (targeted compositions indicated). The insets illustrate HRTEM images for each composition showing lattice fringes and, for $x=1.75$, hollow particle formation.

For $\text{Co}_{1.0}\text{Ni}_{1.0}\text{P}$, Artigas et al. observed that 80.5% of the M(2) sites were occupied by Ni atoms, while only 19.5% of the more spatially confined M(1) sites were occupied by Ni atoms.³⁰ The extent of ordering of the metal atoms in the M(1) and M(2) sites increased with increasing Ni content. Preferential ordering of the metal atoms has been observed for Ni and Fe in bulk and nanoscale $\text{Ni}_{2-x}\text{Fe}_x\text{P}$ materials as measured by Mössbauer spectroscopy.^{32,33}

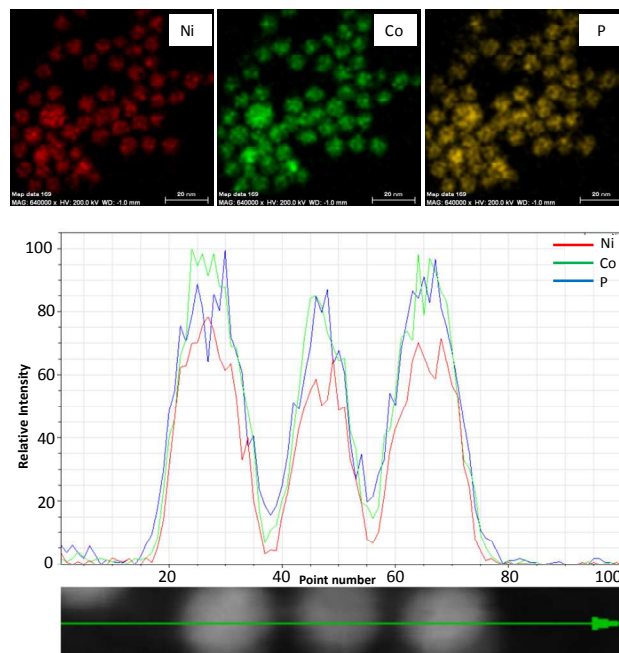


Figure 5. STEM images and elemental mapping data for a $\text{Ni}_{0.67}\text{Co}_{1.33}\text{P}$ sample. In the plot of intensity vs. point number, Ni is shown in red, Co in green and P in blue.

The morphology, particle size and composition of the $\text{Ni}_{2-x}\text{Co}_x\text{P}$ nanoparticle materials were analysed by TEM and EDS, respectively, and the results are shown in Figure 4 and Table 1. The particle sizes are in the range 9-14 nm, slightly larger, but comparable to values obtained from crystallite size analysis of the PXRD data (Table 1). The standard deviations range from ± 5 -18% with greater deviations manifesting for $x > 1.0$.

The particle size distribution histograms with Gaussian profiles are shown in Figure S4 for all compositions. The histograms reveal a larger size distribution of particles for cobalt rich compositions. However, for all compositions the standard deviation is $< \pm 20$. High resolution TEM (HRTEM) images were taken for all compositions and are shown as insets in each TEM image. Lattice planes are evident throughout the crystallites, but at the Co-rich compositions, hollow particles are also observed. The formation of hollow particles may be attributed to the diffusion rate differences between metals and P, according to the Kirkendall effect.³⁴ In previous studies the formation of hollow particles for cobalt phosphides has also been noted,³⁵ suggesting that Co is a highly mobile metal within the phosphide lattice.

In comparing the sizes obtained from PXRD (by application of the Scherrer equation) to TEM (average

from histogram), it is evident that the former method is slightly underestimating the size. This may be due to an amorphous layer on the particle surface, polydispersity of particles and/or the presence of hollow particles for some compositions ($x=1.75$ in Figure 4). Additionally, the TEM size measurement method could be contributing as the software models assume a perfect sphere, but TEM images indicate that some particles are elongated along the a or c axes (see Figure 4 inset, $x = 1.5$).

From the EDS analysis the compositions of the materials were calculated and the metal ratio is found to be close (within 5-20%) to the ratio employed in the synthesis, as shown in Table 1. STEM images and elemental mapping data for the $\text{Ni}_{0.67}\text{Co}_{1.33}\text{P}$ composition show that the two metals are homogeneously distributed within a particle, consistent with solid-solution formation (Figure 5). Overall the developed protocol is ideal to synthesize $\text{Ni}_{2-x}\text{Co}_x\text{P}$ nanoparticles as nearly monodisperse samples ($\pm 20\%$ S.D.)²⁶ with good control of composition in the range $x < 1.7$.

The surfaces of some of the $\text{Ni}_{2-x}\text{Co}_x\text{P}$ compositions ($x = 0, 0.08, 0.25, 0.50$) were probed with XPS and the resulting spectra in the $\text{Ni}(2\text{P}_{3/2})$, $\text{Co}(2\text{P}_{3/2})$ and $\text{P}(2\text{P})$ regions are shown in Figure 6.

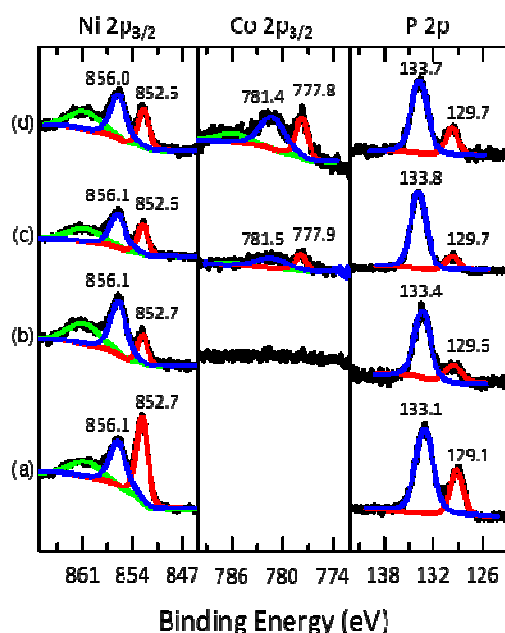


Figure 6. XPS spectra of $\text{Ni}_{2-x}\text{Co}_x\text{P}$ nanoparticle compositions: (a) Ni_2P , (b) $\text{Co}_{0.08}\text{Ni}_{1.92}\text{P}$, (c) $\text{Co}_{0.25}\text{Ni}_{1.75}\text{P}$ and (d) $\text{Co}_{0.50}\text{Ni}_{1.50}\text{P}$ in the $\text{Ni}(2\text{P}_{3/2})$, $\text{Co}(2\text{P}_{3/2})$ and $\text{P}(2\text{P})$ regions.

The binding energies observed for Ni (856.0-856.1 eV), Co (781.4-781.5 eV) and P (133.1-133.8 eV) correspond to the oxidized phase of each component resulting from the oxide layer formation on the nanoparticle surface due to air exposure. Those binding energies noted for each component correspond to Ni^{2+} , Co^{2+} and P^{5+} , respectively.³⁶ The oxide layer is not an issue for catalytic studies as these materials are preheated under reducing conditions prior to catalytic testing. The binding energy

observed for reduced P species (129.1-129.7 eV) is lower than that for the elemental P (129.9-130.2 eV).^{37,38} This is attributed to a higher electron density present in these phosphides caused by transfer of electron density from the metal species to the more electronegative phosphorus. The lower binding energies for P are consistent with previous studies done for $\text{Ni}_2\text{P}/\text{SiO}_2$ and $\text{Co}_2\text{P}/\text{SiO}_2$ materials prepared by temperature-programmed reduction (TPR).³⁹⁻⁴¹ The peaks observed for reduced species of Ni (852.5-852.7 eV) and Co (777.8-777.9 eV) are consistent with the binding energies reported for zero-valent Ni (852.5-852.9 eV) and Co (778.1-778.2 eV).³⁹⁻⁴¹ The $\text{Ni}(2\text{P}_{3/2})$ peak is slightly shifted to lower binding energies (852.7-852.5 eV) with increased Co content suggesting the presence of slightly higher electron density.

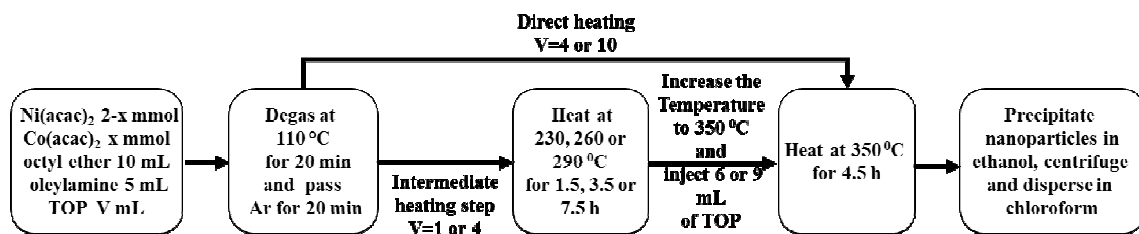
The binding energies for the present ternary phosphide components are in the range of values observed by Bussell and coworkers in their study of TPR-prepared $\text{Ni}_{2-x}\text{Co}_x\text{P}/\text{SiO}_2$.¹⁴ XPS studies were performed for three compositions ($x=0.25, 1.00, 1.75$), but there was no clear pattern in binding energy shifts with increasing cobalt. Mar and co-workers studied the effect of metal substitution for bulk $(\text{Ni}_{1-x}\text{M}_x)_2\text{P}$ ($\text{M}=\text{Cr}, \text{Fe}, \text{Co}$) using XPS and X-ray absorption near-edge spectroscopy (XANES).⁴² By comparing the satellite intensity of $\text{Ni } 2\text{p}_{3/2}$ XPS spectra and the Ni and metal (Cr, Fe, Co) edge XANES spectra, Mar and coworkers concluded that charge transfer from M to Ni does occur in the $(\text{Ni}_{1-x}\text{M}_x)_2\text{P}$ phases, although this is small in magnitude for bulk Ni_2P doped with Co.

The surface compositions of the $\text{Ni}_{2-x}\text{Co}_x\text{P}$ nanoparticles ($x = 0, 0.08, 0.25, 0.50$) were evaluated by XPS and the normalized metal ratios are shown in Table S1. The surface metal compositions closely track those measured by EDS, while the P:M ratios determined by XPS are in the range 2-2.9, indicating that the surfaces are P rich. Surface enrichment in P might be due to the stripping of metal ions from the surface during the nanoparticle washing procedure. The loss of surface metal ions on metal chalcogenide nanoparticles during ligand exchange has been noted by Owen and co-workers.⁴³ It is likely that a similar mechanism is operable here. Intriguingly, in TPR-prepared Ni rich materials the surface compositions were found to be quite P enriched for bulk phase materials ($\text{P}:\text{M} = 1.2\text{-}4.8$),¹⁷ but less so for nanoscale $\text{Ni}_{2-x}\text{Co}_x\text{P}$ particles prepared on a silica support ($\text{P}:\text{M} = 0.51\text{-}0.76$).¹⁴

Mechanistic studies on particle formation: NiCoP

Effect of intermediate heating temperature and heating time on precursor particle formation and templating

Based on our experience with Ni_2P , the initial hypothesis regarding the mechanism of $\text{Ni}_x\text{Co}_{2-x}\text{P}$ particle formation was that an intermediate mixed-metal phase was formed at 230 °C and these particles acted as templates for the final ternary phosphide. To test this hypothesis, intermediate particles were isolated after the synthesis step at 6



Scheme 1. Reaction protocols for the synthesis of Ni_{2-x}Co_xP nanoparticles

230 °C with TOP:M=4.48 (8.96 mmol:2.00 mmol) for a representative composition, Ni:Co=1:1 (Scheme 1). As shown in Figure 7a, precursor particles formed at 230 °C were found to have CoO, NiO or a mixed metal oxide as the only crystalline phase. NiO and CoO are virtually indistinguishable by PXRD but CoO is the more likely impurity phase as we do not see NiO in the binary Ni₂P synthesis.²⁰ Our presumption of CoO formation is also consistent with a study done by Seo et al.⁴⁴ In their work, a reaction protocol of Co(acac)₃ and oleylamine was developed at 200 °C to synthesize two different phases of CoO, presuming the oxygen was contributed by the acetylacetonate ligand in the metal precursor complex. From the TEM image in Figure 7(a), it is evident that while some spherical particles form, much of the product consists of features < 1 nm, most likely nuclei. We do observe an amorphous shell on these particles that may be due to an amorphous layer of reactant species or uncrystallized oxide on the particle surface. Thus, it appears that while nucleation starts at 230 °C, particle growth is incomplete at the 1.5 h mark, unlike the case for pure Ni₂P.²⁰ Nevertheless the final ternary phosphide particles obtained are nearly monodisperse and spherical, as shown in Figure 4.

In order to better understand the chemical and structural changes that occur upon heating the precursor particles to the crystallization temperature (350 °C), the initial reaction temperature was changed from 230 °C to 260 °C and 290 °C and particles were isolated. For the particles heated at 260 °C no CoO was observed in the PXRD pattern (Figure 7b). Instead a broad peak is observed near 44° 2θ that can be indexed to the (111) reflection of fcc Ni (or Co). Based on the breadth of the peak and the absence of any higher order reflections, we presume this to be a metal-P amorphous alloy.^{35,45,46} The absence of CoO is attributed to reduction to fcc Co metal by oleylamine at this temperature, as observed by Nam et al.⁴⁷

When the intermediate temperature was increased to 290 °C, the formation of crystalline NiCoP was observed (Figure 7c), indicating this temperature is sufficient to crystallize the material. The particle size is slightly larger (8.8 nm from the PXRD data and 12.24 ± 1.72 nm from TEM) than that obtained at 350 °C and some hollow particles are observed (Figure 7c). Hollow particle formation for this composition can be attributed to the lower amount of TOP used in the reaction medium relative to the two step

synthesis, where a second aliquot of TOP is added before increasing the temperature to form the crystalline phosphide. When less TOP is present, the concentration of P diffusing into the particles is decreased and the effect of Co-diffusion outward is magnified according to the Kirkendall effect.

Prior studies have shown a strong relationship between the composition and size of the precursor particles and that of the final crystalline phosphide. Robinson and co-workers did a thorough investigation on incorporation of P into Ni nanocrystals, observing that phosphorus incorporation increases with time and temperature.⁴⁵ Accordingly, we sought to investigate the effect of time on particle shape and composition at 230 °C and 260 °C.

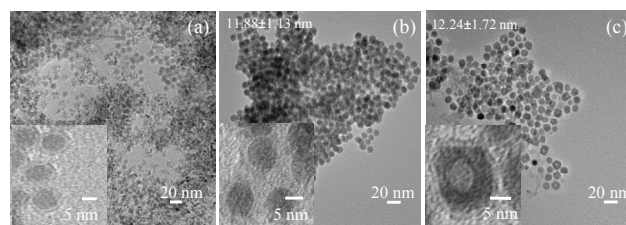
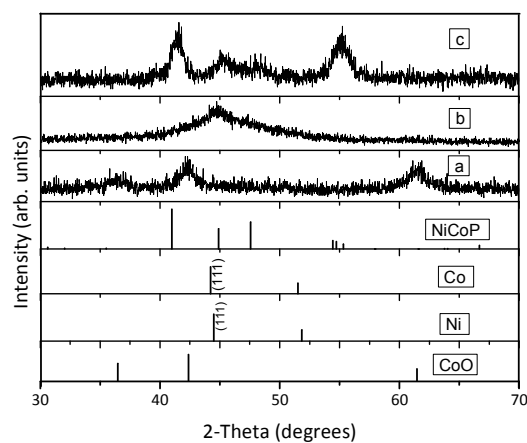


Figure 7. PXRD patterns and TEM images of NiCoP nanoparticles obtained from heating at (a) 230 °C (b) 260 °C (c) 290 °C for 1.5 h with TOP:M=4.48 (reference PXRD patterns for CoO, fcc Ni, Co and for NiCoP are shown). The insets in TEM micrographs show HRTEM images of representative particles

As shown in Figure S5, heating for 1.5 or 3.5 h at 230 °C resulted in CoO as the only detectable phase by PXRD, whereas by 7.5 h the fcc (111) peak manifests as a very broad reflection superposed over peaks for CoO. At the same time, the TEM data show a shift from poorly-defined particles at shorter times to ca 12 nm spherical particles at 7.5 h (Figure S6). EDS analysis was carried out for regions with spherical particles and it was revealed that the P amount increased with time (@1.5 h M:P = 2.4, @3.5 h M:P=5.5, @7.5 h M:P=3.4).

A similar series of reactions was done for precursor particle formation at 260 °C at different time intervals, yielding only the (111) reflection by PXRD and a particle size of (again) ca. 12 nm (Figure S7 and S8). Relative to 230 °C, more P is being incorporated at 260 °C and the extent of incorporation also increases with time (@1.5 h M:P=3.5, @3.5 h M:P=3.2, @7.5 h M:P=2.9). This pattern of P incorporation is similar to that reported by Robinson and co-workers.⁴⁵

To investigate whether spherical precursor particles formed at low temperatures act as templates for the final crystalline ternary phosphide particles, reactions were done by heating at 230 °C and 260 °C for 7.5 h and 1.5 h, respectively, with TOP:M=4.48, and then heated to 350 °C for 4.5 h after injecting an additional 6 mL of TOP, thus modifying only the intermediate step in our standard preparation. In both cases, spherical particles adopting the NiCoP phase were obtained. The size (ca. 13 nm, Figure S9) was slightly larger than the precursor particles (ca. 12 nm, Figure S6, S8), attributed to crystallization and lattice expansion upon inclusion of more P.

Modifying the precursor particles to increase the size

We sought to modify the size of the precursor particles as a means to control the size of the NiCoP product. This was achieved by using a minimum of TOP in the initial synthesis (1 mL of initial TOP to produce TOP:M=1.12) to force formation of crystalline NiCo nanoparticles over Ni-Co-P amorphous alloys (Scheme 1). As shown in Figure 8, when the reaction mixture is heated for 7.5 h at 230 °C, crystalline peaks appeared that could be assigned to the (111) and (200) reflections of fcc Ni-Co alloy, which has a very similar pattern to each of the pure metals as observed by Li et al.⁴⁸ The TEM image indicates the particles are larger (20.63 ± 2.14 nm) compared to reactions using 4 mL of TOP, attributed to the lesser degree of stabilization of the particles' surface. In the isolation process the particles adhered to the stirring bar, suggesting ferromagnetic or superparamagnetic behavior that is indicative of Ni-Co alloys, and not of amorphous Ni-Co-P particles, similar to our previous observations for amorphous Ni-P particles.²⁰

The precursor particles were subsequently converted to the final ternary phosphide phase by introducing a further 9 mL (20.2 mmol) of TOP at 350 °C to make overall TOP:M=11.2. The final ternary phosphide particles obtained have the correct phase and the size of these particles (23.62 ± 2.85) is again similar to the large precursor particles from which they formed, consistent with templated formation (Figure 8). Some hollow particles were also present in the reaction product, attributed to both

the large precursor particle size and the absence of P-incorporation inducing a large diffusion gradient for phosphidation.

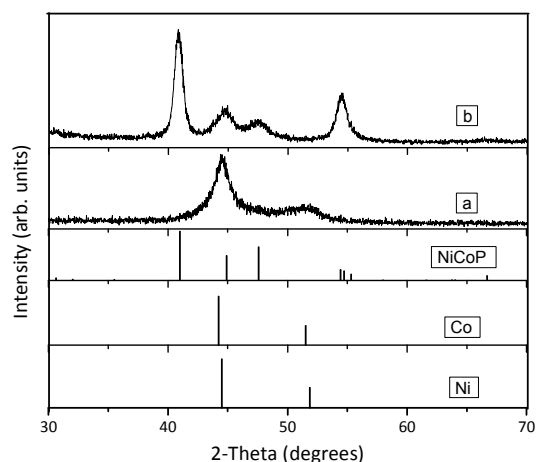


Figure 8. PXRD patterns (reference patterns for Ni, Co, and NiCoP are shown) and TEM images of nanoparticles obtained from reactions (a) initially heated at 230 °C with TOP:M=1.12 for 7.5 h (b) followed by heating at 350 °C for 4.5 h after injection of an additional 20.2 mmol of TOP. The inset shows the enlarged image to highlight the hollow particles.

Further size-control by direct heating to the crystallization temperature

Based on the fact that the 230 °C step at short times does not produce well-formed nanoparticles, precursor particle formation likely occurs *en route* to heating to 350 °C. This led us to question whether the low temperature step is necessary or whether direct heating would be suitable to produce ternary phosphide nanoparticles. To test this hypothesis, the reaction mixture was heated directly to 350 °C with a high initial TOP:M=11.2 (10 mL TOP, Scheme 1). To investigate whether any alloy precursor particles are formed at the initial stage of reaction or whether there is any growth in the particle size with the heating time, particles were isolated at different time intervals at 350 °C. As observed by PXRD, during the time interval 1.5-4.5 h at 350 °C, the phase of materials was consistent with crystalline NiCoP (Figure S10) and the average particle sizes were the same regardless of time intervals investigated, with a low degree of polydispersity, typically $< \pm 10$ % standard deviation (Figure S10). The⁸

size of these particles was smaller (7-8 nm) compared to the particles observed in the approach with the intermediate heating step (ca 12 nm). We expect this is the case because the particle growth takes place in the presence of an excess of TOP which facilitates the stabilization of the surface of the particles, inhibiting the growth. If this is the case, it should be possible to increase the size of the product particles by decreasing the quantity of TOP employed. Accordingly, a direct heating reaction was conducted at 350 °C with 4 mL of TOP (TOP:M=4.48) (Scheme 1). As shown in Figure S11 the particles obtained index to NiCoP in the PXRD and are larger in size (ca 14-15 nm) compared to those obtained from TOP:M=11.2. A consequence of the reduced TOP is, once again, formation of hollows within the spherical NiCoP particles, which accounts for a portion of the increased particle diameter, in addition to the reduced surface stabilization.

Conclusions

A solution-phase synthetic protocol is established for production of Ni_{2-x}Co_xP nanoparticles in the range x≤1.7 as narrow polydispersity samples with control of size, shape, and morphology (dense vs. hollow particles). Composition modulation (x) in the product reflects the starting composition until the very Co-rich end is reached, at which point impurity phases become apparent. Increasing Co-concentration results in an increase in polydispersity and is accompanied by formation of voids within the solid particles due to the Kirkendall effect. A comprehensive study of the role of key parameters on particle formation and growth of the NiCoP phase reveals that precursor particles formed below the crystallization temperature act as templates for the final crystalline product. At low M:P ratios the precursor particles are amorphous metal phosphides of small size (< 10 nm) that transform to dense particles, whereas at high M:P ratios, the precursor particles are large (> 20 nm) crystalline NiCo alloy particles that transform to large hollow NiCoP particles. Formation of precursor particles by a moderate temperature soak is not *a priori* a requirement for NiCoP particle formation. Direct heating to the crystallization temperature also results in narrow polydispersity samples with size controllable by the M:P ratio. The ability to tune the particle size, composition and morphology in Ni_{2-x}Co_xP opens the door to an understanding of how these factors impact the catalytic function.

Supporting information

NMR spectrum for oleylamine, particle size histograms, PXRD patterns and TEM images of intermediate particles heated at 230 °C and 260 °C for different time intervals, crystalline particles obtained by conversion of intermediate particles, and particles directly heated to the crystallization temperature (figures); surface composition of Ni_{2-x}Co_xP nanoparticles assessed by XPS (table). This material is available free of charge via the internet at <http://pubs.acs.org>.

Author Information

Corresponding author

*E-mail: sbrock@chem.wayne.edu

Funding

This material is based upon work supported by the National Science Foundation under Grant Nos. 1361702, 1361741 (CHE) and 1064159 (DMR).

Acknowledgment

HAADF/STEM data were acquired on a FEI Titan 80-200 field emission transmission electron microscope with ChemiSTEM technology purchased with funds provided by NSF MRI award 1040588, the Murdock Charitable Trust and Oregon Nanoscience and Microtechnologies Institute (ONAMI). TEM and HRTEM data were acquired on a JEOL 2010 TEM with funds provided by NSF MRI award 0216084. TEM, NMR and powder X-ray diffraction were acquired at the Lumigen Instrument Center, Wayne State University. The XPS analyses were performed at the Surface Analysis Recharge Center (SARC) at the University of Washington. We thank Akhila Kuda Wedagedara and Jessica Davis for their assistance with NMR.

References

- (1) Souza, D.; Pralong, V.; Jacobson, A.; Nazar, L. A Reversible Solid-State Crystalline Transformation in a Metal Phosphide Induced by Redox Chemistry. *Science* **2002**, *296*, 2012-2015.
- (2) Xie, R.; Battaglia, D.; Peng, X. Colloidal InP Nanocrystals as Efficient Emitters Covering Blue to Near-Infrared. *J. Am. Chem. Soc.* **2007**, *129*, 15432-15433.
- (3) Brock, S. L.; Perera, S. C.; Stamm, K. L. Chemical Routes for Production of Transition-Metal Phosphides on the Nanoscale: Implications for Advanced Magnetic and Catalytic Materials. *Chem. - Eur. J.* **2004**, *10*, 3364-3371.
- (4) Prins, R.; Bussell, M. E. Metal Phosphides: Preparation, Characterization and Catalytic Reactivity. *Catal. Lett.* **2012**, *142*, 1413-1436.
- (5) Carenco, S.; Portehault, D.; Boissière, C.; Mézailles, N.; Sanchez, C. Nanoscaled Metal Borides and Phosphides: Recent Developments and Perspectives. *Chem. Rev.* **2013**, *113*, 7981-8065.
- (6) Popczun, E. J.; McKone, J. R.; Read, C. G.; Biacchi, A. J.; Wiltrout, A. M.; Lewis, N. S.; Schaak, R. E. Nanostructured Nickel Phosphide as an Electrocatalyst for the Hydrogen Evolution Reaction. *J. Am. Chem. Soc.* **2013**, *135*, 9267-9270.
- (7) Callejas, J. F.; McEnaney, J. M.; Read, C. G.; Crompton, J. C.; Biacchi, A. J.; Popczun, E. J.; Gordon, T. R.; Lewis, N. S.; Schaak, R. E. Electrocatalytic and Photocatalytic Hydrogen Production from Acidic and Neutral-pH Aqueous Solutions Using Iron Phosphide Nanoparticles. *ACS Nano* **2014**, *8*, 1101-1107.
- (8) McEnaney, J. M.; Crompton, J. C.; Callejas, J. F.; Popczun, E. J.; Biacchi, A. J.; Lewis, N. S.; Schaak, R. E. Amorphous Molybdenum Phosphide Nanoparticles for Electrocatalytic Hydrogen Evolution. *Chem. Mater.* **2014**, *26*, 4826-4831.
- (9) McEnaney, J. M.; Crompton, J. C.; Callejas, J. F.; Popczun, E. J.; Read, C. G.; Lewis, N. S.; Schaak, R. E. Electrocatalytic Hydrogen Evolution Using Amorphous Tungsten Phosphide Nanoparticles. *Chem. Commun.* **2014**, *50*, 11026-11028.
- (10) Popczun, E. J.; Read, C. G.; Roske, C. W.; Lewis, N. S.;

Schaak, R. E. Highly Active Electrocatalysis of the Hydrogen Evolution Reaction by Cobalt Phosphide Nanoparticles. *Angew. Chem. Int. Ed.* **2014**, *53*, 5427-5430.

(11) Xiao, P.; Sk, M. A.; Thia, L.; Ge, X.; Lim, R. J.; Wang, J.-Y.; Lim, K. H.; Wang, X. Molybdenum Phosphide as an Efficient Electrocatalyst for the Hydrogen Evolution Reaction. *Energy Environ. Sci.* **2014**, *7*, 2624-2629.

(12) Oyama, S. T. Novel Catalysts for Advanced Hydroprocessing: Transition Metal Phosphides. *J. Catal.* **2003**, *216*, 343-352.

(13) Sun, F.; Wu, W.; Wu, Z.; Guo, J.; Wei, Z.; Yang, Y.; Jiang, Z.; Tian, F.; Li, C. Dibenzothiophene Hydrodesulfurization Activity and Surface Sites of Silica-Supported MoP, Ni₂P, and NiMoP Catalysts. *J. Catal.* **2004**, *228*, 298-310.

(14) Burns, A. W.; Gaudette, A. F.; Bussell, M. E. Hydrodesulfurization Properties of Cobalt-Nickel Phosphide Catalysts: Ni-Rich Materials are Highly Active. *J. Catal.* **2008**, *260*, 262-269.

(15) Ding, L.; Shu, Y.; Wang, A.; Zheng, M.; Li, L.; Wang, X.; Zhang, T. Preparation and Catalytic Performances of Ternary Phosphides NiCoP for Hydrazine Decomposition. *Appl. Catal., A* **2010**, *385*, 232-237.

(16) Lu, A.; Chen, Y.; Li, H.; Dowd, A.; Cortie, M. B.; Xie, Q.; Guo, H.; Qi, Q.; Peng, D.-L. Magnetic Metal Phosphide Nanorods as Effective Hydrogen-Evolution Electrocatalysts. *Int. J. Hydrogen Energy* **2014**, *39*, 18919-18928.

(17) Abu, I. I.; Smith, K. J. The Effect of Cobalt Addition to Bulk MoP and Ni₂P Catalysts for the Hydrodesulfurization of 4, 6-Dimethylbenzothiophene. *J. Catal.* **2006**, *241*, 356-366.

(18) Park, J.; Koo, B.; Yoon, K. Y.; Hwang, Y.; Kang, M.; Park, J.-G.; Hyeon, T. Generalized Synthesis of Metal Phosphide Nanorods via Thermal Decomposition of Continuously Delivered Metal-Phosphine Complexes Using a Syringe Pump. *J. Am. Chem. Soc.* **2005**, *127*, 8433-8440.

(19) Henkes, A. E.; Vasquez, Y.; Schaak, R. E. Converting Metals into Phosphides: A General Strategy for the Synthesis of Metal Phosphide Nanocrystals. *J. Am. Chem. Soc.* **2007**, *129*, 1896-1897.

(20) Muthuswamy, E.; Savithra, G. H. L.; Brock, S. L. Synthetic Levers Enabling Independent Control of Phase, Size, and Morphology in Nickel Phosphide Nanoparticles. *ACS Nano* **2011**, *5*, 2402-2411.

(21) Mobarok, M. H.; Luber, E. J.; Bernard, G. M.; Peng, L.; Wasylishen, R. E.; Buriak, J. M. Phase-Pure Crystalline Zinc Phosphide Nanoparticles: Synthetic Approaches and Characterization. *Chem. Mater.* **2014**, *26*, 1925-1935.

(22) Layan Savithra, G. H.; Bowker, R. H.; Carrillo, B. A.; Bussell, M. E.; Brock, S. L. Mesoporous Matrix Encapsulation for the Synthesis of Monodisperse Pd₅P₂ Nanoparticle Hydrodesulfurization Catalysts. *ACS Appl. Mater. Interfaces* **2013**, *5*, 5403-5407.

(23) Layan Savithra, G. H.; Muthuswamy, E.; Bowker, R. H.; Carrillo, B. A.; Bussell, M. E.; Brock, S. L. Rational Design of Nickel Phosphide Hydrodesulfurization Catalysts: Controlling Particle Size and Preventing Sintering. *Chem. Mater.* **2013**, *25*, 825-833.

(24) Yoon, K. Y.; Jang, Y.; Park, J.; Hwang, Y.; Koo, B.; Park, J.-G.; Hyeon, T. Synthesis of Uniform-Sized Bimetallic Iron-Nickel Phosphide Nanorods. *J. Solid State Chem.* **2008**, *181*, 1609-1613.

(25) Ye, E.; Zhang, S.-Y.; Lim, S. H.; Bosman, M.; Zhang, Z.; Win, K. Y.; Han, M.-Y. Ternary Cobalt-Iron Phosphide Nanocrystals with Controlled Compositions, Properties, and Morphologies from Nanorods and Nanorice to Split Nanostructures. *Chem. - Eur. J.* **2011**, *17*, 5982-5988.

(26) Aiken Iii, J. D.; Lin, Y.; Finke, R. G. A Perspective on Nanocluster Catalysis: Polyoxoanion and (n-C₄H₉)₄N⁺ Stabilized Ir(o)~300 Nanocluster 'Soluble Heterogeneous Catalysts'. *J. Mol. Catal. A: Chem.* **1996**, *114*, 29-51.

(27) Sénateur, J. P.; Rouault, A.; L'Héritier, P.; Krumbügel-Nylund, A.; Fruchart, R. Fruchart, D.; Convert, P.; Roudaut, E., La Selectivite des Substitutions dans les Phases MM'P Etude de L'ordre par Diffraction Neutronique dans NiCoP. *Mater. Res. Bull.* **1973**, *8*, 229-238.

(28) Fruchart, R.; Roger, A.; Senateur, J. P. Crystallographic and Magnetic Properties of Solid Solutions of the Phosphides M₂P, M = Cr, Mn, Fe, Co, and Ni. *J. Appl. Phys.* **1969**, *40*, 1250-1257.

(29) Fruchart, R. Effets d'Electronegativite et Interactions Metalliques dans les Phosphures et Arseniures Ternaires des Elements de Transition 3d, 4d, 5d de Type Metallique. *Ann. Chim. Fr.* **1982**, *7*, 563-604.

(30) Artigas, M.; Bacmann, M.; Boursier, D.; Fruchart, D.; Fruchart, R.; Soubeyroux, J. L. Formation of Diamagnetic Metal Clusters in the Metallic System Nickel Phosphide (Ni₂P)-Cobalt Phosphide (Co₂P). *Comptes Rendus de l'Academie des Sciences, Serie II: Mecanique, Physique, Chimie, Sciences de la Terre et de l'Univers* **1992**, *315*, 29-34.

(31) Huheey, J. E.; Keiter, E. A.; Keiter, R. L. *Inorganic Chemistry: Principles of Structure and Reactivity*; 4th ed.; Harper Collins College Publishers: NY, 1993.

(32) Maeda, Y.; Takashima, Y. Mössbauer Studies of FeNiP and Related Compounds. *J. Inorg. Nucl. Chem.* **1973**, *35*, 1963-1969.

(33) Gaudette, A. F.; Burns, A. W.; Hayes, J. R.; Smith, M. C.; Seda, T.; Bussell, M. E. Mössbauer Spectroscopy Investigation and Hydrodesulfurization Properties of Iron-Nickel Phosphide Catalysts. *J. Catal.* **2010**, *272*, 18-27.

(34) Chiang, R.-K.; Chiang, R.-T. Formation of Hollow Ni₂P Nanoparticles Based on the Nanoscale Kirkendall Effect. *Inorg. Chem.* **2006**, *46*, 369-371.

(35) Ha, D.-H.; Moreau, L. M.; Bealing, C. R.; Zhang, H.; Hennig, R. G.; Robinson, R. D. The Structural Evolution and Diffusion During the Chemical Transformation from Cobalt to Cobalt Phosphide Nanoparticles. *J. Mater. Chem.* **2011**, *21*, 11498-11510.

(36) Korányi, T. Phosphorus Promotion of Ni (Co)-Containing Mo-Free Catalysts in Thiophene Hydrodesulfurization. *Appl. Catal., A* **2003**, *239*, 253-267.

(37) *Practical Surface Analysis by Auger and X-ray Photoelectron Spectroscopy*; Briggs, D.; Seah, M. P., Eds.; John Wiley & Sons: NY, 1983; Appendix 4, pp 477-533.

(38) Blanchard, P. E. R.; Grosvenor, A. P.; Cavell, R. G.; Mar, A. X-ray Photoelectron and Absorption Spectroscopy of Metal-Rich Phosphides M₂P and M₃P (M = Cr-Ni). *Chem. Mater.* **2008**, *20*, 7081-7088.

(39) Sawhill, S. J.; Layman, K. A.; Van Wyk, D. R.; Engelhard, M. H.; Wang, C.; Bussell, M. E. Thiophene Hydrodesulfurization over Nickel Phosphide Catalysts: Effect 10

1 of the Precursor Composition and Support. *J. Catal.* **2005**, *231*,
2 300-313.

3 (40) Sawhill, S. J.; Phillips, D. C.; Bussell, M. E. Thiophene
4 Hydrodesulfurization over Supported Nickel
5 Phosphide Catalysts. *J. Catal.* **2003**, *215*, 208-219.

6 (41) Burns, A. W.; Layman, K. A.; Bale, D. H.; Bussell, M. E.
7 Understanding the Relationship between Composition and
8 Hydrodesulfurization Properties for Cobalt Phosphide Catalysts.
9 *Appl. Catal., A* **2008**, *343*, 68-76.

10 (42) Blanchard, P. E. R.; Grosvenor, A. P.; Cavell, R. G.; Mar, A.
11 Effects of Metal Substitution in Transition-Metal Phosphides
12 ($\text{Ni}_{1-x}\text{M}'_x$)₂P (M' = Cr, Fe, Co) Studied by X-ray Photoelectron and
13 Absorption Spectroscopy. *J. Mater. Chem.* **2009**, *19*, 6015-6022.

14 (43) Anderson, N. C.; Hendricks, M. P.; Choi, J. J.; Owen, J. S.
15 Ligand Exchange and the Stoichiometry of Metal Chalcogenide
16 Nanocrystals: Spectroscopic Observation of Facile Metal-
17 Carboxylate Displacement and Binding. *J. Am. Chem. Soc.* **2013**,
18 *135*, 18536-18548.

19 (44) Seo, W. S.; Shim, J. H.; Oh, S. J.; Lee, E. K.; Hur, N. H.;
20 Park, J. T. Phase- and Size-Controlled Synthesis of Hexagonal
21 and Cubic CoO Nanocrystals. *J. Am. Chem. Soc.* **2005**, *127*, 6188-
22 6189.

23 (45) Moreau, L. M.; Ha, D.-H.; Bealing, C. R.; Zhang, H.;
24 Hennig, R. G.; Robinson, R. D. Unintended Phosphorus Doping
25 of Nickel Nanoparticles during Synthesis with TOP: A Discovery
26 through Structural Analysis. *Nano Lett.* **2012**, *12*, 4530-4539.

27 (46) Wang, J.; Johnston-Peck, A. C.; Tracy, J. B. Nickel
28 Phosphide Nanoparticles with Hollow, Solid, and Amorphous
29 Structures. *Chem. Mater.* **2009**, *21*, 4462-4467.

30 (47) Nam, K. M.; Shim, J. H.; Ki, H.; Choi, S.-I.; Lee, G.; Jang, J.
31 K.; Jo, Y.; Jung, M.-H.; Song, H.; Park, J. T. Single-Crystalline
32 Hollow Face-Centered-Cubic Cobalt Nanoparticles from Solid
33 Face-Centered-Cubic Cobalt Oxide Nanoparticles. *Angew. Chem.*
34 *Int. Ed.* **2008**, *47*, 9504-9508.

35 (48) D. Li, Y.; Q. Li, L.; W. Liao, H.; R. Wang, H. Preparation
36 of Pure Nickel, Cobalt, Nickel-Cobalt and Nickel-Copper Alloys
37 by Hydrothermal Reduction. *J. Mater. Chem.* **1999**, *9*, 2675-2677.

